UNIVERSIDAD COMPLUTENSE DE MADRID

FACULTAD DE CIENCIAS FÍSICAS

Máster en Meteorología y Geofísica

TRABAJO DE FIN DE MÁSTER

Relación entre el Jet Stream Subtropical y la generación de vientos y oleajes en superficie en la costa oeste de Sudamérica

Relationship between the Subtropical Jet Stream and the generation of Surface Winds and Swells along the Western Coast of South America

Gonzalo Agurto Barragán

Tutores:

Dr. Ricardo García Herrera

Dr. Soledad Collazo Inglesini

Curso académico 2024-2025

Calificación: 9.2

Abstract

Extreme swell episodes along the Pacific coast of South America are low-frequency but high-impact phenomena that often originate from distant synoptic disturbances in the South Pacific. These events have the potential to disrupt port operations, fisheries, and coastal infrastructure, particularly when they reach a "very strong" intensity. For instance, the anomalous swell of May 2023 led to flooding and maritime restrictions across several Peruvian localities. Between 2008 and 2023, Peru's Directorate of Hydrography and Navigation (DIHIDRONAV) issued more than 820 abnormal swell warnings, with only 1% categorized as "very strong" due to their exceptional intensity and impact.

This study focuses on the atmospheric conditions associated with these high-impact events, particularly the role of upper-tropospheric dynamics. Using reanalysis data and internal records from DIHIDRONAV, five "very strong" swell events recorded during the austral winter (May–September) were selected for analysis. The methodology integrates synoptic composites, principal component analysis (PCA), and Euclidean distance metrics to assess vertical coherence and anomaly magnitude across multiple pressure levels. Furthermore, a multiparametric jet stream diagnostic is applied for a detailed characterization of the upper-level atmospheric circulation.

The results indicate that extreme swell events are preceded by a vertically aligned and dynamically mature baroclinic structure that extends from the surface to the upper troposphere. At 250 hPa, the polar front jet exhibits significantly higher intensity, sharper wind gradients, and enhanced zonal persistence compared to climatology, supporting its role as a modulating factor in swell generation. Moreover, PCA and Euclidean distance analyses suggest the unusual nature of these events—especially aloft—relative to multidecadal climatology. These findings underscore the importance of upper-level dynamics in driving ocean–atmosphere interactions and provide a basis for improving early-warning systems in the region.

Acknowledgments

This work would not have been possible without the instruction, guidance, and dedication of the professors, fellow students, and academic coordinators at the Faculty of Physical Sciences of the Complutense University of Madrid (UCM), whom I had the great privilege of meeting during my studies and who helped me deepen my understanding of the fascinating world of meteorology.

I am especially grateful to my supervisors, Dr. Soledad Collazo and Dr. Ricardo García Herrera, for their patience and unwavering support throughout the preparation of this work, as well as for their invaluable lessons and insights along the way.

I also wish to express my sincere appreciation to my home institution, the Directorate of Hydrography and Navigation of the Peruvian Navy, for providing access to essential data and technical advice that helped shape this study into a contribution toward enhancing marine meteorological monitoring capabilities.

Finally, I extend my deepest thanks to my family, and to my beloved father in heaven, who remain my constant source of inspiration and motivation.

Table of contents

1. Introduction and objectives 1
1.1 Introduction 1
1.2 Objectives 2

2. Data and Methodology 2

3. Results 6
3.1 Atmospheric circulation related to Extreme Wave Events 6
3.2 Multilevel Analysis of Dominant Atmospheric Patterns using PCA 8
3.3 Multiparametric Analysis of Jet Stream 15

4. Conclusions 18

References 20

Appendix A: Sequences of Wind Fields at 250 hPa, Geopotential Height at 500 hPa, Surface Pressure, and Surface Wind 21

Appendix B: Time Series of Principal Components from Surface Pressure, 500 hPa Geopotential, and 250 hPa Geopotential Fields 24

1. Introduction and objectives

1.1 Introduction

Extreme swell events along the western coast of South America pose recurrent risks to coastal populations, infrastructure, and maritime operations. Although they often originate from distant disturbances in the South Pacific, their impacts can be substantial. For instance, the anomalous swell of May 2023 caused flooding, port closures, and damage along the Peruvian coast, prompting the issuance of special warnings and the temporary suspension of fishing and recreational activities (Infobae, 2023).

Peru's Directorate of Hydrography and Navigation (DIHIDRONAV) has systematically monitored and issued abnormal swell warnings, where each event is classified by intensity—light, moderate, strong, or very strong—based on wave height relative to normal conditions. According to internal records (Directorate of Hydrography and Navigation, 2023), a total of 823 swell warnings were issued between 2008 and 2023. Of these, 78 corresponded to strong or very strong swells, with only five events reaching the "very strong" category. Despite their low frequency (1%), these high-intensity cases are of particular concern due to their disproportionate impacts. Notably, around 80% of all swells originated from the southwest, reinforcing the influence of long-period waves driven by large-scale ocean–atmosphere disturbances in the South Pacific. This is consistent with regional wave climatology described by Aguirre et al. (2017), who analyzed a 32-year hindcast (1980–2012) and satellite altimetry to characterize mean wave conditions in the Southeast Pacific. Their results revealed a marked seasonal cycle, with higher significant wave heights during the austral winter and a prevailing swell direction from the southwest along most of the western coast of South America. These conditions reflect the dominant influence of swell generated by extratropical storms in the Southern Ocean, with little interannual variability in average wave height during the study period.

The generation of these events is commonly associated with persistent and intense wind fields over the southeastern Pacific. However, swell occurrence in the region is also influenced by broader climatological patterns of atmospheric circulation. The southeastern Pacific is characterized by the interaction between the semi-permanent South Pacific Subtropical High and frequent extratropical cyclones in mid to high latitudes. These features control the seasonal distribution of wave energy and swell propagation pathways. Alves (2006) demonstrated that long-period swell in the Pacific Ocean is primarily generated by extratropical storms, which can transmit energy over thousands of kilometers with little dissipation. These background atmospheric conditions enable the development of swell events under relatively stable forcing, while specific synoptic configurations—such as the presence of quasi-stationary fronts—can greatly intensify wave generation. As Campos Caba (2016)

notes, "swells on the southwestern coast of South America are mainly produced by distant storms in the South Pacific, with favorable conditions for their formation in the presence of quasi-stationary fronts more than 3,200 km from the coast and with multiple frontal situations, which would ensure extensive and long-lasting wind fields." However, the specific atmospheric configurations responsible for initiating and maintaining these swells—particularly in the upper troposphere—are still not fully understood.

1.2 Objectives

Although several studies have examined swell generation and propagation in the Southeast Pacific (e.g., (Alves, 2006); (Campos Caba, 2016); (Aguirre et al., 2017)), to our knowledge, no previous research has explicitly addressed the role of upper-level atmospheric circulation in modulating extreme swell events along the Pacific coast of South America. In particular, the influence of jet stream dynamics and vertical synoptic coherence remains insufficiently explored from a climatological perspective. For this reason, the main objective of this study is:

- To analyze the synoptic-scale atmospheric patterns—particularly in the upper troposphere associated with very strong swell events affecting the Pacific coast of South America, with a focus on their structure, coherence, and potential for swell generation.

To achieve this, the study addresses the following specific objectives:

- To characterize the vertical alignment and baroclinic structure of extreme events using composite analysis of geopotential height and wind fields at different pressure levels.
- To identify dominant synoptic modes and assess the relative anomaly of each case by applying principal component analysis (PCA) and Euclidean distance metrics .
- To examine the configuration of the upper-level jet stream through a multiparametric diagnostic during extreme events.
- To determine whether upper-level patterns offer consistent signals that could improve the anticipation and understanding of high-impact swell events.

2. Data and Methodology

For this study, anomalous swell events affecting the western coast of South America were identified using information provided by the DIHIDRONAV, the institution responsible for issuing special warnings of anomalous swells and winds for the Area of Responsibility XVI (METAREA XVI) of the Global Maritime Distress and Safety System (GMDSS). These datasets include the number of special swell and wind warnings issued between 2008 and 2023, along with their respective intensities,

start and end dates. Specifically, this study used data on extreme events categorized as "very strong" during the austral cold season (May–September), according to the classification established by the Directorate of Hydrography and Navigation (2025), as shown in Table 1 below:

Event	Year	Special Warning Number	Start date	End date	Maximum swell intensity	Direction
E1	2011	31	19/06/2011	24/06/2011	Very strong	S / SW
E2	2014	28	01/07/2014	04/07/2014	Very strong	S / SW
E3	2017	61-62	11/08/2017	15/08/2017	Very strong	S / SW
E4	2017	68	07/09/2017	11/09/2017	Very strong	S / SW
E5	2023	26	27/05/2023	30/05/2023	Very strong	S / SW

Table 1: *"Very strong" events from 2008 to 2023, indicating the year of occurrence, warning number, start and end dates, intensity, and direction of origin. According to the DIHIDRONAV classification, a "very strong" swell implies wave heights exceeding three times their normal conditions. In contrast, "light" intensity indicates wave heights around 0.5 times the normal, "moderate" intensity up to twice the normal, and "strong" intensity between two and three times the normal wave heights.*

As a first step, the sequences of atmospheric conditions that led to the generation of these swells in the Southeastern Pacific were analyzed. For this, the theory of deep-water wave propagation (Stewart, 2008) was used to estimate the approximate travel time of the wave group to the Peruvian coast and to observe the conditions on the days prior to the swell's arrival, based on the dates provided in Table 1. According to the Department of Oceanography at DIHIDRONAV, "the intensity and duration of swell depend on the evolution, orientation, and distance of the atmospheric disturbance, mainly the persistence of the winds" (Otiniano, 2006). In this regard, southwest swells can be detected 2 to 5 days in advance from the wind-disturbance zone known as the "fetch".

Based on this information, the wind generation sequences prior to anomalous swells for the events listed in Table 1 were obtained from ERA5 reanalysis by the European Centre for Medium-Range Weather Forecasts (Hersbach et al., 2020), represented through maps of wind fields at 250 hPa, geopotential height at 500 hPa, sea level pressure, and surface winds from one day before the onset of the "very strong" swells (Figures A1–A5 in Appendix A). To support this, Equation 1 shows the calculation of the arrival time "t" (in seconds) as a function of the distance "X" (in meters) from the source to the observation point, the group wave period "T", gravitational acceleration (9.81 m/s^2), and the constant "pi".

$$t = \frac{4\pi X}{gT} \tag{1}$$

Taking as reference the average point calculated from the fetch generation regions for the anomalous events on the surface wind maps (see Table A1 in Appendix A) and another point off the southern coast of Peru in the NE direction (coordinates: 15.4ºS, 75.18ºW), a distance of 4,035 kilometers was obtained. Additionally, a wave period between 16 and 20 seconds was considered,

as observed in the case study of anomalous southwest swell conducted by Tamayo Infantes (2007). With this data, an average travel time between 72 and 90 hours was obtained, equivalent to 3 to 3.75 days prior to the occurrence of the anomalous swell, allowing focus on the atmospheric conditions that gave rise to extreme swells around those dates. It is worth noting that in some cases, travel times may be shorter than these intervals due to factors such as the interaction of the swell with the Humboldt Current, which flows in the same direction as the swell propagation and may increase the effective speed of the wave train by acting as an additional carrier, shortening the arrival time without necessarily increasing the wave period (Holthuijsen, 2007).

Subsequently, based on daily reanalysis data from 1991 to 2023 from ERA5 (Hersbach et al., 2020), composite maps of geopotential height and its anomalies were constructed for the five extreme events (E1–E5) at the 250 and 500 hPa levels. Additionally, composites of wind fields (magnitude and direction) and their anomalies were generated at the 250 and 1000 hPa levels. These products aimed to characterize the average synoptic behavior preceding the anomalous swell events and assess whether structural consistency existed among the events. To this end, a multi-level analysis (from the surface to upper levels) was performed to account for baroclinic instability, a key driver of mid-latitude cyclogenesis. This instability modulates wind fields within cyclonic systems, which subsequently generate surface swells through sustained energy transfer to the ocean. Python was used in the JupyterLab development environment, where the composites were calculated by averaging the four days preceding each of the five extreme events. The seasonal climatological mean field (May to September 1991–2020) was subtracted from this average to obtain the anomaly maps.

To determine whether the differences observed between extreme events and climatology were statistically significant, the non-parametric Mann–Whitney U test (Mann & Whitney, 1947) was applied using the *mannwhitneyu* function from the *scipy.stats* module (Virtanen et al., 2020). This test evaluates whether the distributions of atmospheric fields (such as wind and geopotential height) during extreme events differ significantly from their climatological values at each point in the analyzed domain.

Next, to identify dominant patterns of spatial and temporal variability in the atmospheric fields, Principal Component Analysis (PCA) was applied to the same daily reanalysis data. This technique was applied separately to geopotential height and surface pressure fields. Prior to PCA, daily anomalies were calculated by subtracting the monthly climatology at each grid point. Each map was then reshaped so that each grid point became an individual variable, and the PCA algorithm automatically centered the data (i.e., it removed the temporal mean at each grid point) before performing the analysis.

This analysis was implemented using the scikit-learn library in Python, allowing the extraction of the main components (EOFs) and their respective time series (scores or PCs). From these, regression and correlation maps with the original fields were generated to identify recurring synoptic structures and possible atmospheric drivers associated with anomalous swell events. The Mann–Whitney U

test was also applied point by point to the spatial data, identifying regions where anomalies were statistically significant ($p < 0.05$) on the maps, thus providing physical relevance to the patterns obtained through PCA.

Additionally, to evaluate the statistical representativeness of extreme events within the space defined by the principal components, the Euclidean distance was calculated between each day from 1991 to 2023 and the centroid defined by the average of all days (climatological), in the multidimensional space formed by the first eight principal components (PC1–PC8). This analysis was conducted independently for the geopotential height fields at 500 and 250 hPa, as well as for surface pressure. Subsequently, histograms of the Euclidean distances were created for each level, allowing visualization of the dispersion and relative rarity of extreme events with respect to the entire dataset. This statistical tool helped quantify how far these events deviate from multiyear climatological behavior, providing further evidence of their exceptional nature.

Finally, to further characterize and understand the jet stream configuration in the Southern Hemisphere during these events, a multiparametric analysis of the jet stream in the Southeastern Pacific sector (140°W–70°W) was performed. For this, daily zonal wind data at 250 hPa from ERA5 were used, and the methodology developed by Collazo et al. (2024) was applied in order to have a better representation of upper-level jet features. In fact, this approach overcomes the limitations of traditional analysis based solely on jet latitude and intensity by incorporating additional metrics describing its dynamic structure, such as tilt, sharpness, meridional displacement (departure), number of branches, and longitudinal extension. From the daily calculation of these diagnostic parameters, values were extracted and grouped according to the event category: climatology, light, moderate, and extreme swell events. Boxplots and scatter plots were then produced to analyze the distributions and relationships among the different parameters, differentiating the signal associated with extreme events from the climatological behavior.

Moreover, non-parametric statistical tests were applied to assess whether the observed differences between categories were statistically significant. Specifically, the Mann–Whitney U test was used to test whether the distributions of jet parameters during extreme events differed significantly from general climatology. Likewise, the Kolmogorov–Smirnov test (Smirnov, 1948), implemented via the *ks_2samp* function from the *scipy.stats* module (Virtanen et al., 2020), was applied to compare the cumulative distribution functions of both samples and detect differences in shape, location, or dispersion. Both tests were applied individually to each diagnostic parameter and provided a statistical basis to interpret the uniqueness of jet stream configurations associated with extreme swell events.

3. Results

3.1 Atmospheric circulation related to Extreme Wave Events

To begin with, we examine the large-scale atmospheric circulation patterns associated with extreme wave events using composite analyses. Figure 1 illustrates a negative sea level pressure (SLP) anomaly off the southern coast of Chile (subpolar low), accompanied by a positive anomaly over the South Atlantic and another one to the northwest, the latter associated with the Southeast Pacific Subtropical Anticyclone (SPSA). It is worth noting that the SPSA, which is semi-permanently located off the western coast of South America, plays a fundamental role in regional circulation by modulating wind direction and intensity and contributing to the transport of subtropical air masses toward midlatitudes (Flores-Aqueveque et al., 2020). In this context, the configuration indicates a strengthening of the SPSA, amplifying the pressure gradient between the anticyclone and the subpolar low and favoring an anomalous southwesterly wind flow. The composite map of 1000 hPa winds shows an enhancement of cyclonic circulation, with wind direction consistent with the circulation induced by the pressure anomalies and strong winds in the region with intense gradients between the SPSA and the subpolar low. Wind intensity anomalies confirm this strengthening, with values exceeding +4 m/s particularly southwest of Chile, where the pressure gradient is strongest. Meanwhile, wind direction anomalies highlight a cyclonic circulation (clockwise) near the Chilean coast and an anticyclonic pattern (counterclockwise) over the open ocean, reflecting the interaction between the subpolar low and the strengthened SPSA.

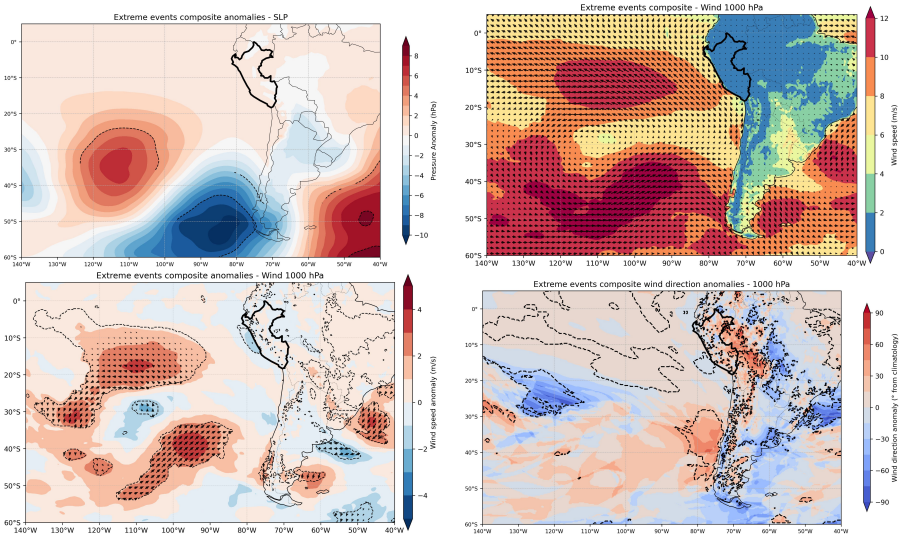

Figure 1: *Composite maps of sea level pressure (SLP) anomalies (top left), 1000 hPa wind vectors (top right), 1000 hPa wind intensity anomalies (bottom left), and 1000 hPa wind direction anomalies (bottom right), calculated as the average over the four days preceding the five extreme events (E1–E5). The outline of Peru is highlighted in bold black to emphasize the coastal region analyzed.*

To better understand the vertical structure of this circulation system, Figure 2 presents the corresponding mid-tropospheric composite. The geopotential height anomalies at 500 hPa reveal a pronounced negative anomaly nearly aligned with the surface low, flanked by positive anomalies to the west and east. This tripolar configuration is consistent with patterns typically associated with the propagation of planetary Rossby waves, which modulate mid-tropospheric circulation and favor the intensification of extratropical synoptic systems (Müller & Ambrizzi, 2007). The vertical coherence between surface and mid-level anomalies—indicative of a barotropically aligned structure that results from the mature stage of a baroclinic wave—suggests that the disturbance had already passed its baroclinic growth phase. The absence of the westward tilt with height that is typical of developing baroclinic systems reinforces this interpretation, pointing to a later, possibly decaying stage of the baroclinic life cycle. Thus, the composite anomalies at both levels jointly depict a vertically stacked, mature synoptic system responsible for the anomalous surface wind forcing that ultimately contributed to the generation of extreme swell events.

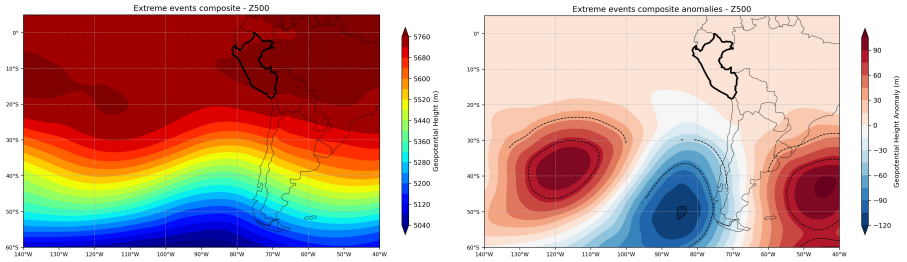

Figure 2: *Composite maps of 500 hPa geopotential height (left) and its anomalies (right), calculated as the average over the four days preceding the five extreme events (E1–E5). For the anomaly map, the seasonal climatological mean (May–September) from 1991 to 2023 was subtracted. The outline of Peru is highlighted in bold black to emphasize the coastal region analyzed.*

In the upper troposphere, Figure 3 presents the composite anomalies at 250 hPa, providing further evidence of the vertically coherent nature of the synoptic disturbance. The geopotential height anomalies exhibit a pronounced negative center southwest of South America, closely aligned with the mid-tropospheric and surface lows, and flanked by positive anomalies to the west and east. The composite of total wind at 250 hPa reveals the core of the subtropical jet stream extending over 35°–42°S, with maximum speeds exceeding 45 m/s along its axis. In particular, the wind speed anomalies exhibit local enhancements of up to +16 m/s along the northwestern flank of the upper-level cyclonic anomaly, near 100°W–40°S, suggesting a localized jet streak that may be dynamically linked to the system's evolution. Meanwhile, the wind direction anomalies show a marked cyclonic curvature around the base of the negative pole, consistent with the anomalous circulation observed at lower levels.

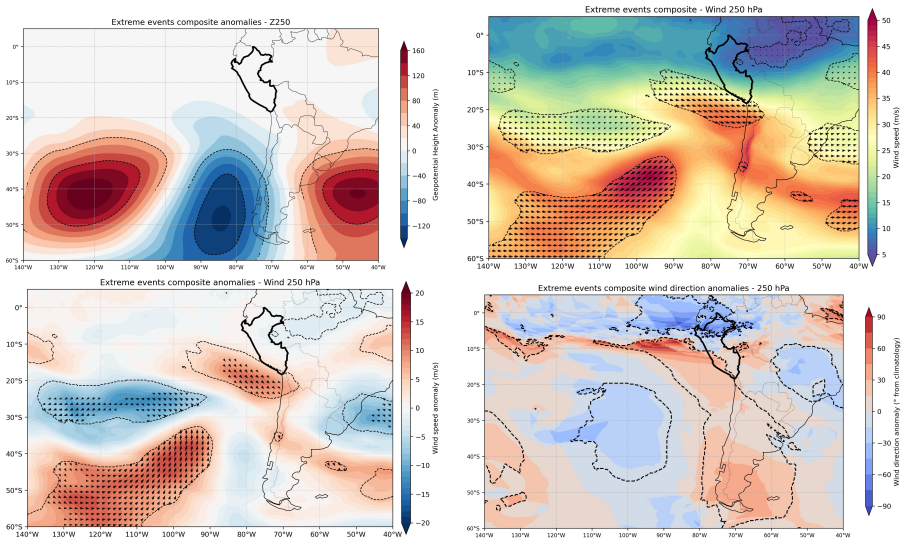

Figure 3: *Composite maps of 250 hPa geopotential height anomalies (top left), 250 hPa wind vectors (top right), 250 hPa wind intensity anomalies (bottom left), and 250 hPa wind direction anomalies (bottom right), calculated as the average over the four days preceding the five extreme events (E1–E5). The outline of Peru is highlighted in bold black to emphasize the coastal region analyzed.*

Altogether, the upper-level features support the vertical coherence of the mature baroclinic wave identified earlier. The symmetric wind anomalies, lack of divergence aloft, and absence of westward tilt further support the interpretation of a vertically stacked, non-growing disturbance.

3.2 Multilevel Analysis of Dominant Atmospheric Patterns using PCA

To complement the composite analysis and identify the dominant modes of synoptic variability, PCA was applied to daily anomalies of sea level pressure (SLP) and geopotential height fields over the study region during MJJS (1991–2023). Unlike composites, which highlight average anomalies, PCA allows the extraction of recurrent spatial patterns (EOFs) and their temporal evolution (PCs), helping to assess their relevance during extreme events.

Figure 4 displays the regression maps for the first two EOFs. In detail, EOF1 (24.14% of the explained variance) captures a meridional dipole structure with a positive center over the South Atlantic and a negative center over the southeastern Pacific, consistent with the climatological configuration of the subpolar low-pressure belt. EOF2 (10.06%), on the other hand, shows a spatial pattern that more closely resembles the composite anomaly presented in Figure 1, with a negative anomaly off the southern coast of Chile and a positive anomaly over the South Atlantic, suggesting a strengthened pressure gradient between the South Pacific Anticyclone and the subpolar low.

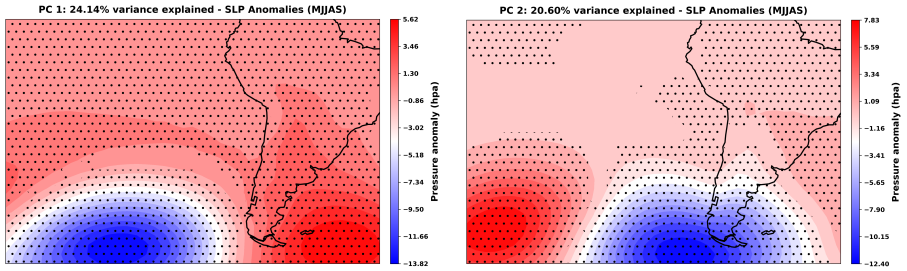

Figure 4: *Regression maps corresponding to the first two Principal Components (PC1 and PC2) of the daily sea level pressure (SLP) anomaly field, calculated for the months of May through September (MJJS) from 1991 to 2023. Stippled areas indicate statistical significance ($p < 0.05$) based on the Mann–Whitney U test.*

The remaining EOFs (EOF3 to EOF8) are also shown in Appendix B - Figure B1; although they capture additional variance, they mostly reflect horizontal or dipolar structures not directly aligned with the composite pattern associated with extreme events. In particular, EOF3 and EOF4 depict a nearly zonal alternation between low and high pressure in the Southeastern Pacific, but lack clear surface signatures relevant to swell generation from the southwest direction. EOF5 through EOF8 exhibit meridionally elongated anomalies with limited spatial coherence and inconsistent activation across events.

The temporal projection of the first eight principal components (PC1–PC8) during the extreme events is shown in Figure B2 (see Appendix B) and summarized in Table 5. In particular, PC2 consistently exhibits the highest values among all components during events E2 and E5, specifically reaching 2.07 in E5 and 1.88 in E2. This temporal activation reinforces the spatial coherence previously noted for EOF2, supporting its relevance as a dominant surface-level mode associated with the extreme events. PC5, by contrast, shows the most negative values in the entire dataset, especially during E3 (–3.89) and E1 (–2.94). These extreme projections indicate that both events are strongly associated with a pattern similar in structure but opposite in sign to EOF5. As shown in Figure 4, EOF5 presents an inverse dipolar pressure anomaly that intensifies the zonal pressure gradient and may favor northeasterly winds. Therefore, the opposite-phase projection during E3 and E1 would be consistent with southwesterly flow conditions conducive to swell generation in the region shown in the SLP anomalies of Figure 1.

The remaining components display lower and more variable values across events, without a clear temporal pattern. While PCs 1, 3, and 4 occasionally show elevated values, their corresponding EOFs lack spatial alignment with the composite anomaly pattern and do not display consistent activation during the events, limiting their interpretive value in this context.

To further assess how exceptional the extreme events are in relation to the overall synoptic variability and quantify how far each daily configuration deviates from the average state, Figure 5 presents the results of the Euclidean distance histogram. It shows that three of the extreme events

	PC1	PC2	PC3	PC4	PC5	PC6	PC7	PC8
E1	-0.593	-0.287	-0.389	0.691	**-2.935**	-1.058	-0.498	-1.041
E2	1.268	**1.884**	0.512	0.914	0.961	1.487	0.327	-1.244
E3	0.325	0.153	1.372	-0.313	**-3.891**	0.089	1.244	-1.540
E4	0.953	1.179	0.039	**1.819**	-0.336	0.714	0.367	-0.705
E5	0.364	**2.068**	0.993	0.342	-0.482	0.371	0.832	-0.760

Table 2: *Values corresponding to the five extreme events (E1–E5) for each of the first eight principal components (PC1–PC8) of the daily sea level pressure (SLP) anomaly field, calculated for the months of May to September (MJJS) between 1991 and 2023. Bold values indicate the highest component score for each individual event.*

(E1–E5) fall within the upper end of the distribution, two above the 80th percentile (E1, E2), and one surpassing the 99th percentile (E3). The other two events are close to the median (E4, E5). These results suggest that the SLP synoptic configuration observed during E1 and E2, although not sufficient by itself, may represent a necessary condition for the generation of anomalous swells, as only a subset of the extreme cases aligns with markedly atypical circulation patterns in the surface pressure field.

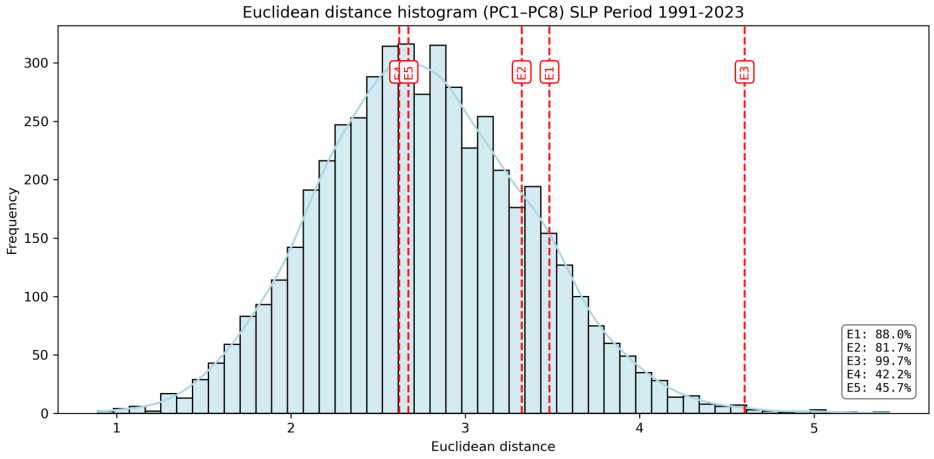

Figure 5: *Histogram of Euclidean distances from each day in the 1991–2023 period to the climatological centroid (mean of all days), calculated in the space of the first eight SLP principal components (PC1–PC8) of the sea level pressure (SLP) field for the MJJS months. Dashed red lines represent the five selected extreme events (E1–E5), whose percentiles are shown in the lower right panel.*

The same analysis was repeated for the geopotential height anomalies at 500 hPa, yielding similar results in terms of dominant patterns and explained variance.

In Figure 6, EOF1 (24.06% of explained variance) represents a large-scale pattern characterized by a meridional structure between the southeastern Pacific and South America, reflecting the dominant planetary wave configuration at mid-levels. However, EOF2 (20.20%) shows a closer spatial match with the composite pattern previously described (Figure 2), displaying a deep trough extending from the Pacific toward southeastern South America, flanked by two positive anomaly centers. This

structure resembles a Rossby wave pattern typical of the MJJS season, characterized by enhanced meridional flow.

Beyond EOF2, the subsequent modes (EOF3 to EOF8) account for additional mid-tropospheric variability but exhibit spatial structures that differ from the composite anomaly associated with extreme events (see Figure B3 in Appendix B). EOF3 and EOF4 reflect broad wave-like patterns typical of planetary-scale dynamics, while EOF5 through EOF8 present more fragmented or meridionally extended anomalies with limited coherence.

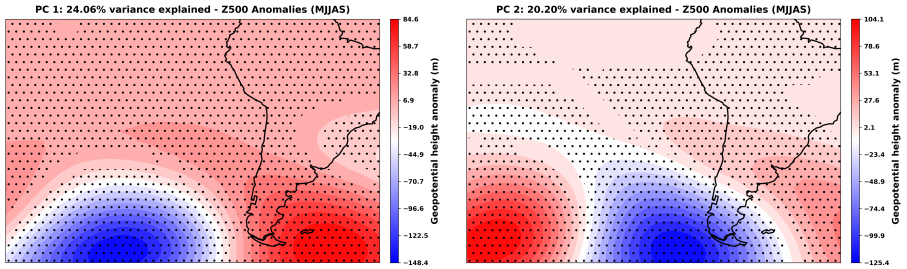

Figure 6: *Regression maps corresponding to the first two Principal Components (PC1 and PC2) of the daily 500 hPa geopotential height anomaly field, calculated for the MJJS months between 1991 and 2023. Stippled areas indicate statistical significance ($p < 0.05$) based on the Mann–Whitney U test.*

From a temporal standpoint (Figure B4, Appendix B), the projection values of the first eight principal components (PC1–PC8) during the extreme events are summarized in Table 6. PC2 reaches its highest value during event E5 (2.84) and remains elevated in E2 (1.45), confirming its role as the dominant mode consistently activated during at least two major events. PC4 also shows notable projections in E1 (2.39), E3 (1.53), and E4 (1.98), suggesting a recurrent, though not universal, contribution. The circulation pattern associated with EOF4 differs from that of EOF2, primarily in the positioning of the low-pressure center, which shifts further north. This displacement creates a pressure gradient oriented toward the northwest, resulting in southeastward flow over the subtropical Pacific. Such a configuration appears to be less favorable for the generation of southwest swells affecting the Peruvian coast; however, this assessment requires caution due to the prevalence of wind shear (directional variation with altitude), a common feature of mid-latitude atmospheric dynamics.

Other components, such as PC1 or PC3, display elevated values in isolated cases but lack both spatial correspondence with the composite anomaly and consistent activation across events. Overall, PC2 emerges as the most relevant mid-tropospheric signal, with PC4 representing a secondary mode that may be linked to alternative synoptic evolutions or less effective swell-generating conditions.

	PC1	PC2	PC3	PC4	PC5	PC6	PC7	PC8
E1	-1.237	0.464	-0.240	**2.390**	-1.407	-1.116	-0.691	-0.558
E2	**1.903**	1.445	0.215	1.048	0.868	0.916	-1.229	0.968
E3	0.204	0.659	1.170	1.527	**-2.452**	-1.946	1.029	-1.206
E4	1.090	1.037	-0.961	**1.982**	0.980	-0.420	0.378	1.458
E5	1.080	**2.840**	0.267	0.568	-0.450	-0.462	0.939	1.513

Table 3: *Values corresponding to the five extreme events (E1–E5) for each of the first eight principal components (PC1–PC8) of the daily 500 hPa geopotential height anomaly field, calculated for the months of May to September (MJJS) between 1991 and 2023. Bold values indicate the highest component score for each individual event.*

The corresponding histogram (Figure 7) reinforces these findings, showing that all five extreme events fall within the upper tail of the distance distribution. Notably, event E3 once again stands out as a highly exceptional case, reaching the 99th percentile—consistent with its distinct projection in the PCA space. Events E1 and E5 also appear above the 80th percentile, suggesting that the mid-tropospheric configuration may act as a necessary, though not sufficient, condition for swell generation. In contrast, E4 and E2 lie closer to the median of the distribution, indicating that not all extreme events are associated with highly unusual circulation patterns at this level. These results indicate that, in terms of mid-tropospheric circulation, the selected events represent markedly unusual configurations in some cases, but not universally across all events.

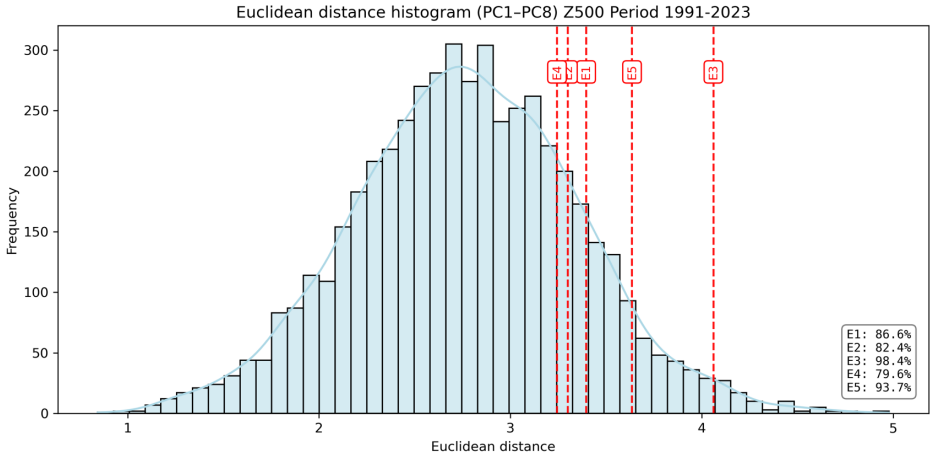

Figure 7: *Histogram of Euclidean distances from each day in the 1991–2023 period to the climatological centroid (mean of all days), calculated in the space of the first eight principal components (PC1–PC8) of the 500 hPa geopotential height field for the MJJS months. Dashed red lines represent the five selected extreme events (E1–E5), with their percentiles shown in the lower right panel.*

In Figure 8, EOF1 (21.87% of explained variance) captures the dominant meridional structure of the Z250 field during MJJS, similar to the leading modes identified at lower levels. Likewise, EOF2 (18.78%) most closely resembles the composite anomaly pattern described in Figure 3 and shares

structural features with EOF2 at 500 hPa—particularly the large-scale trough extending over South America. This similarity reinforces the vertical coherence of the synoptic disturbance, consistent with a baroclinically mature configuration.

From a temporal perspective, Table 7 summarizes the projection of the upper-level principal components (PC1–PC8) during the five extreme events (shown in detail in Figure B6, Appendix B). PC2 stands out in event E5, showing the most negative value of the entire dataset (–3.07), reinforcing its relevance as the leading mode associated with that case—also supported by its spatial resemblance to the composite anomaly pattern (Figure 8).

Meanwhile, PC3 exhibits distinctly low values in E1, E2, and especially E3 (–1.92), suggesting a relevant contribution of its associated pattern, which in the spatial maps reflects a northward shift of the trough. PC4 reaches its minimum during E4 (–2.37), a case that may be linked to the synoptic pattern shown in EOF4, where the pressure gradient is oriented more northwestward and the trough is displaced northward—an upper-level configuration that appears less favorable for extreme swell generation. Again, this interpretation should be taken with caution, as vertical wind shear may lead to differences between upper-level and surface wind directions. PC7 and PC8 also display notably high values during E4 and E5, consistent with their spatial patterns featuring meridional structures that could complement the dominant modes.

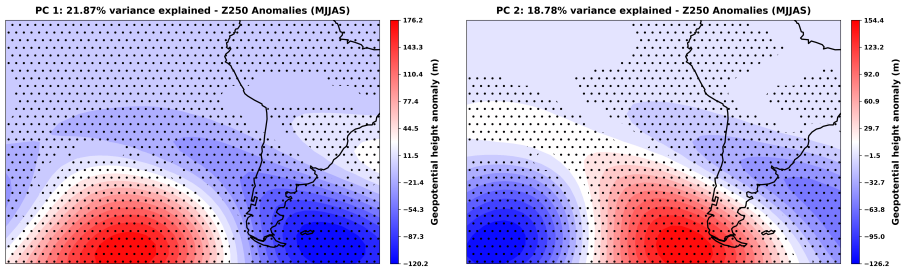

Figure 8: *Regression maps corresponding to the first two Principal Components (PC1 and PC2) of the daily 250 hPa geopotential height anomaly field, calculated for the MJJS months between 1991 and 2023. Stippled areas indicate statistical significance ($p < 0.05$) based on the Mann–Whitney U test.*

Altogether, the temporal projection confirms that while PC2 emerges as the most relevant mode for event E5, other events are shaped by the activation of multiple components. This highlights that extreme upper-level conditions do not follow a single dominant pattern, but instead result from different combinations of EOFs, each with distinct spatial signatures.

	PC1	PC2	PC3	PC4	PC5	PC6	PC7	PC8
E1	1.487	-0.843	-1.696	-1.637	-0.513	-1.066	-0.361	-0.888
E2	**-2.112**	-1.148	-1.261	-0.779	0.881	0.133	-0.985	1.040
E3	-0.026	-0.772	**-1.920**	-0.743	**-1.742**	**-2.017**	1.103	-1.371
E4	-0.910	-0.834	-0.711	**-2.373**	1.304	-0.889	0.856	**1.939**
E5	-1.349	**-3.071**	-0.210	-0.755	-0.318	-0.346	**1.506**	1.382

Table 4: *Values corresponding to the five extreme events (E1–E5) for each of the first eight principal components (PC1–PC8) of the daily 250 hPa geopotential height anomaly field, calculated for the months of May to September (MJJS) between 1991 and 2023. Bold values indicate the highest component score for each individual event.*

Figure 9 presents the histogram of Euclidean distances in the PCA space at 250 hPa, showing that all extreme events fall above the 80th percentile, with E5 reaching up to the 97th percentile. Notably, events such as E4—despite not standing out in the surface-level PCA—appear among the most extreme configurations aloft. This contrast highlights the presence of upper-level anomalies even in cases with more moderate surface signals, reinforcing the vertical complexity of these events and providing further motivation to investigate the role of the upper-level jet in their development. Yet, these histograms should be interpreted with caution, as the PCA at a single level does not account for the vertically coherent structure (from the surface up to 250 hPa) that characterizes these events. Their extreme nature arises from this deep coupling, which the distance metric alone cannot fully capture.

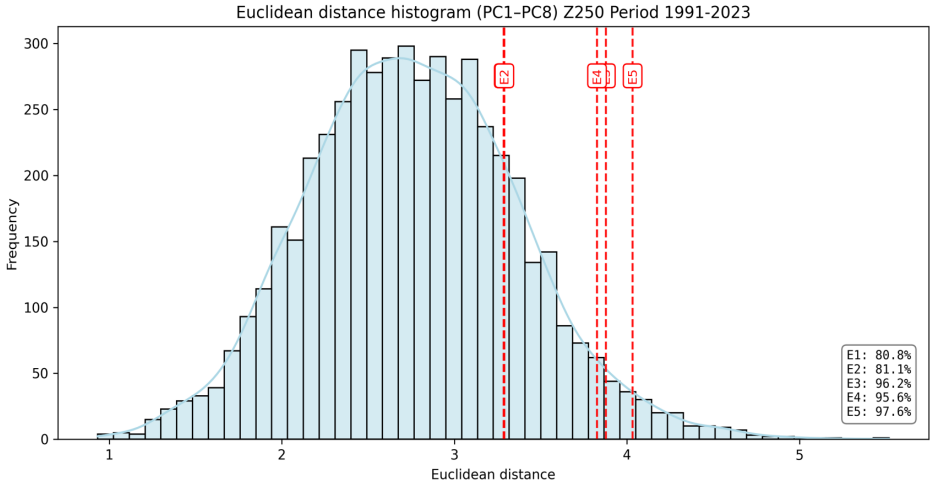

Figure 9: *Histogram of Euclidean distances from each day in the 1991–2023 period to the climatological centroid (mean of all days), calculated in the space of the first eight principal components (PC1–PC8) of the 250 hPa geopotential height field for the MJJS months. Dashed red lines represent the five selected extreme events (E1–E5), with their percentiles shown in the lower right panel.*

3.3 Multiparametric Analysis of Jet Stream

Building on the previous evidence that extreme events are associated with vertically coherent anomalies extending from the surface to the upper troposphere, this section further examines the role of upper-level circulation. In this context, the jet stream emerges as a key element shaping the atmospheric structure, and its configuration is analyzed here using a multiparametric approach designed to capture its main dynamic features.

The first step was to compare the values of various jet stream parameters between the extreme events and the climatological sample using significance tests (Table 8). Some parameters were computed from the total wind field, while others were derived from the zonal mean of the wind field for both the Subtropical Jet (STJ) and the Polar Front Jet (PFJ), following the method of Collazo et al. (2024). This distinction enabled the characterization of both large-scale and transient components of the jet structure. It also served as an initial filter to identify the parameters with a significant influence in characterizing the jet during the days preceding the extreme events.

Zonal mean parameters					**Total wind parameters**				
Climatology vs Extreme	**Intensity STJ**	**Sharpness STJ**	**Departure STJ**	**Lat. STJ**	**Tilting STJ**	**Max. Lat. STJ**	**Max. Lon. STJ**	**Lon. Ext. STJ**	**Max. Int. STJ**
P-value (Mann–Whitney)	0.269	0.482	0.169	0.769	0.870	0.338	0.022	0.887	0.956
P-value (ks_2samp)	0.399	0.519	0.100	0.219	0.781	0.114	0.162	0.877	0.424
Statistically significant (p<0.05)	NO	NO	NO	NO	NO	NO	NO	NO	NO
Median diff. (E–C)	-4.3 m/s	-2.0 m/s	-3.27°	-0.5°	-0.01°/°	-5.5°	21°	0.5°	1.59 m/s

Zonal mean parameters							**Total wind parameters**				
Climatology vs Extreme	**Intensity PFJ**	**Sharpness PFJ**	**Departure PFJ**	**Lat. PFJ**	**Latn. PFJ**	**Lats. PFJ**	**Tilting PFJ**	**Max. Lat. PFJ**	**Max. Lon. PFJ**	**Lon. Ext. PFJ**	**Max. Int. PFJ**
P-value (Mann–Whitney)	**0.032**	**0.023**	**0.010**	0.823	0.972	0.744	**0.072**	0.937	0.146	0.316	0.453
P-value (ks_2samp)	**0.042**	**0.016**	**0.009**	0.690	0.512	0.660	**0.026**	0.580	0.153	0.871	0.305
Statistically significant (p<0.05)	**YES**	**YES**	**YES**	NO	NO	NO	**YES**	NO	NO	NO	NO
Median diff. (E–C)	**7.88 m/s**	**7.68 m/s**	**-4.3°**	1.0°	2.0°	1.5°	**0.12°/°**	-1.0°	-10.5°	4.5°	9.13 m/s

Table 4: *Comparative table of significance values (p-values) between climatology and extreme events for subtropical (top) and polar (bottom) jet parameters. Values were obtained using the Mann–Whitney and Kolmogorov–Smirnov tests (mannwhitneyu, ks_2samp). The last row shows the difference between medians (Extreme minus Climatology). Parameters with statistically significant differences ($p < 0.05$) are shown in bold.*

This analysis revealed statistically significant differences in both the median (Mann–Whitney test) and the overall distribution (Kolmogorov–Smirnov test) for the intensity, sharpness, and departure parameters of the PFJ. For the tilting parameter, although the difference in medians between the climatology and extreme events was not statistically significant at the 95% confidence level ($p = 0.072$, Mann–Whitney U), the Kolmogorov–Smirnov test did indicate a significant difference in the overall distribution ($p = 0.026$).

In terms of magnitude, the median intensity of the PFJ increased by +7.88 m/s during extreme events compared to the climatology, indicating a substantially stronger jet under such conditions. Similarly, sharpness increased by +7.68 m/s, suggesting a significantly more abrupt horizontal wind gradient around the jet core. The departure value, on the other hand, decreased by –4.3°, indicating that the jet core was more tightly aligned with the zonal-mean wind during extreme events, reflecting a more organized and coherent jet structure compared to the climatological state. Although the tilting parameter did not show a significant median difference (delta = +0.12°), the distribution shift supports a tendency toward a more northeastward orientation of the jet axis in extreme cases.

Following the exclusion of non-significant parameters, Figure 10 presents boxplots comparing the values of each PFJ parameter between the general climatology and events classified as light, moderate, and extreme. These additional categories were introduced to evaluate whether the behavior of the selected parameters varies systematically with the intensity of swell events, and to explore if jet parameters evolve progressively with the swell intensity, from climatological to extreme conditions.

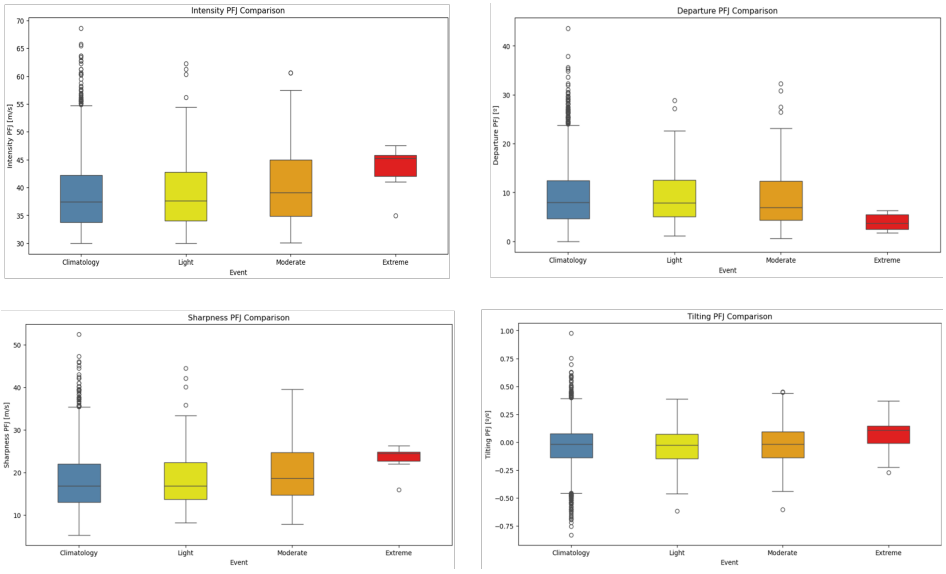

Figure 10: *Boxplots comparing polar front jet (PFJ) parameters for light, moderate, and extreme events, as well as climatology, based on daily 250 hPa zonal wind data from the ERA5 reanalysis. Parameters with statistically significant differences (p-value < 0.05) between extreme events and climatology—determined via the Mann-Whitney U and Kolmogorov–Smirnov tests—are shown: intensity (top left), departure (top right), sharpness (bottom left), and tilting (bottom right).*

- **Intensity:** During extreme events, the PFJ exhibits consistently higher intensity values com-

pared to climatology, with a median above 45 m/s. This shift toward higher intensities suggests a systematic strengthening of the polar jet under extreme conditions, which is sustained by the presence of horizontal thermal gradients at low and mid-levels according to the thermal wind balance.

- **Departure:** Extreme events show significantly lower departure values compared to climatology, indicating that the jet tends to greater zonal persistence and reduced meandering during extreme cases, which could facilitate more efficient channeling of disturbances toward midlatitudes.

- **Sharpness:** A notable increase in PFJ sharpness is observed during extreme events, with a more concentrated distribution and higher median. This implies that the horizontal wind gradient around the jet core becomes more intense and abrupt, typically associated with well-defined frontal structures and enhanced potential for low-level cyclone development.

- **Tilting:** Although the medians do not differ as markedly as in the other parameters, the Kolmogorov–Smirnov test reveals significant differences in the tilting parameter distribution. During extreme events, tilting values are more positive and less dispersed, suggesting a preference for a southwest-to-northeast orientation of the jet axis.

The multiparametric analysis reveals a coherent signal across several jet stream characteristics during extreme swell events. The PFJ exhibits significantly higher intensity and sharpness values, reflecting a stronger and more defined jet core. These features are consistent with the 250 hPa composite maps, which show localized jet streaks and enhanced horizontal wind gradients along the base of the upper-level cyclonic anomaly. The observed reduction in departure values indicates a jet stream with more zonal persistence and efficient wave guidance—an interpretation supported by the vertically stacked anomaly patterns in the composites and the stable configuration captured by EOF2. Although tilting shows only marginal differences in the median, its distribution shift suggests a preferred southwest-to-northeast orientation of the jet axis during extreme events, in line with the structure of the upper-level trough seen in both the composites and EOF2. Altogether, these parameter changes reinforce the presence of a mature baroclinic setting that has evolved into a vertically coherent and dynamically stable upper-level structure—providing favorable conditions for sustained energy transfer and swell generation.

In order to visualize the interactions between key parameters, Figure 11 displays bivariate scatterplots for selected pairs, highlighting the location of the five extreme events (in red) relative to the climatological sample (in light blue). Although 10 days from the five extreme events were analyzed, only six appear in the scatter plots due to missing values in some parameters. Only complete data pairs were plotted to ensure consistency without altering the dataset.

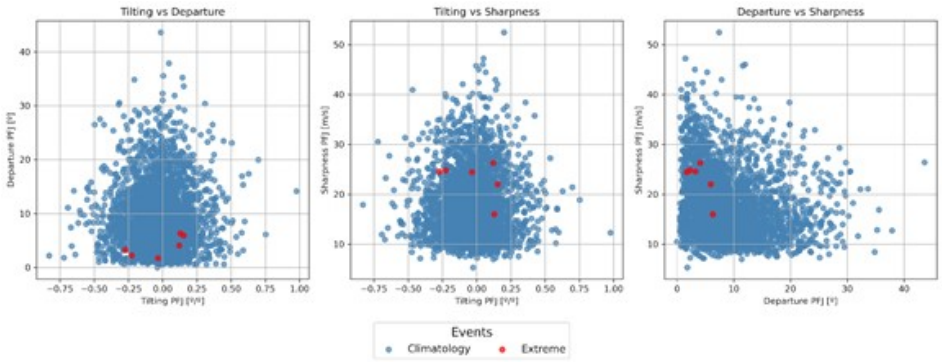

Figure 11: *Comparative scatter plots of polar jet parameters for extreme events and climatology, based on daily 250 hPa zonal wind data from the ERA5 reanalysis. The scatter plots include: tilting vs. departure (left), tilting vs. sharpness (center), and departure vs. sharpness (right).*

In general, there is no clear relationship between the parameters during extreme wave events, nor is there a combination of outliers of the two parameters. However, it is important to point out that few events were analyzed. In the first scatterplot (tilting vs. departure), although extreme events consistently occur at relatively low departure values, it is observed that as the absolute value of the tilting parameter increases, the departure tends to rise slightly.

The second plot (tilting vs. sharpness) shows that extreme events with intermediate to high sharpness values (around 25 m/s) are associated with a wide range of tilting values, both positive and negative. In contrast, when the jet is weaker, extreme swell events appear to occur only when accompanied by positive tilting, suggesting that a certain orientation may compensate for reduced jet intensity.

Finally, in the departure vs. sharpness plot, the extreme events stand out for being concentrated in the area of lower latitudinal dispersion and greater sharpness. However, the plot also suggests that when sharpness decreases, a slight increase in latitudinal spread is needed for an event to reach extreme levels. This pattern supports the idea that, during the most intense events, the polar jet tends to adopt a more compact and well-defined structure.

4. Conclusions

This study aimed to investigate the synoptic atmospheric configurations associated with extreme swell events affecting the western coast of South America, with particular emphasis on the role of mid- and upper-level circulation patterns. The main findings are summarized below:

a) Composite results reveal a vertically stacked and dynamically mature synoptic system, with coherent anomalies from the surface up to 250 hPa. The alignment of geopotential lows across all levels, the absence of westward tilt with height, and the upper-level wind patterns—including

a localized jet streak—indicate a baroclinic wave that has reached its mature stage. This configuration favors sustained surface wind forcing over the ocean, ultimately linked to the generation of extreme swell events along the western coast of South America.

b) PCA analysis supports the presence of a vertically coherent synoptic structure during extreme swell events, with SLP EOF2 emerging as the dominant surface anomaly pattern. Its strong temporal activation in key events, especially E5, highlights the vertical coherence of the synoptic disturbance, consistent with the upper-level anomalies revealed in the PCA and distance analysis. The Euclidean distance metric further underscores the exceptional nature of several cases, particularly in the upper troposphere, though not all events showed the same degree of deviation from climatology.

c) Lastly, the multiparametric characterization of the upper-level jet stream confirms and complements the synoptic patterns identified through composites and EOFs. During extreme swell events, the Polar Front Jet (PFJ) exhibits a significantly stronger, sharper, and low latitudinal deviation configuration, with a preferential southwest-to-northeast tilt. These statistically significant changes emphasize the role of the PFJ as a key modulating factor in the development and persistence of extreme swell conditions over the southeastern Pacific.

d) To further advance our understanding of the jet stream's role in modulating extreme wave events, additional research is warranted. Expanding the analysis to include a larger number of cases—including moderate events or those near the extreme threshold— could help identify additional circulation patterns or thresholds, thereby enhancing early-warning capabilities in support of monitoring agencies in the region. An extended version of this work is being submitted to Journal of Geophysical Research: Oceans.

References

Aguirre, C., Rutllant, J. A., & Falvey, M. (2017). Wind waves climatology of the southeast pacific ocean. *International Journal of Climatology*, *37*(9), 4288–4301. https://doi.org/10.1002/joc.5084

Alves, J.-H. G. (2006). Numerical modeling of ocean swell contributions to the global wave climate. *Ocean Modelling*, *11*(1–2), 98–122. https://doi.org/10.1016/j.ocemod.2004.11.007

Campos Caba, R. V. (2016). Análisis de marejadas históricas y recientes en las costas de chile [Memoria de Título, Ingeniero Civil Oceánico, Universidad de Valparaíso]. https://ingenieriaoceanica.uv.cl/images/stories/Memorias/2016/2016-08-11_CAMPOS_RODRIGO-DEFENSA.pdf

Collazo, S., García-Herrera, R., & Barriopedro, D. (2024). Summer upper-level jets modulate the response of south american climate to enso. *Climate Dynamics*, *62*(3–4), 1031–1054. https://doi.org/10.1007/s00382-023-06955-9

Directorate of Hydrography and Navigation. (2023). Internal swell and wind warning records (2008–2023) [Dirección de Hidrografía y Navegación, Marina de Guerra del Perú. Unpublished internal database].

Directorate of Hydrography and Navigation. (2025). *Avisos especiales*. https://www.dhn.mil.pe/portal/avisos-especiales

Flores-Aqueveque, V., Rojas, M., Aguirre, C., Arias, P. A., & González, C. (2020). South pacific subtropical high from the late holocene to the end of the 21st century: Insights from climate proxies and general circulation models. *Climate of the Past*, *16*, 79–99. https://doi.org/10.5194/cp-16-79-2020

Hersbach, H., Bell, B., Berrisford, P., Hirahara, S., Horányi, A., Muñoz-Sabater, J., Nicolas, J., Peubey, C., Radu, R., Schepers, D., Simmons, A., Soci, C., Abdalla, S., Abellan, X., Balsamo, G., Bechtold, P., Biavati, G., Bidlot, J., Bonavita, M., & Thépaut, J.-N. (2020). The era5 global reanalysis. *Quarterly Journal of the Royal Meteorological Society*, *146*(730), 1999–2049. https://doi.org/10.1002/qj.3803

Holthuijsen, L. H. (2007). *Waves in oceanic and coastal waters*. Cambridge University Press. https://doi.org/10.1017/CBO9780511618536

Infobae. (2023, May). *Oleaje anómalo llegará a su punto pico este fin de semana en la costa peruana, advierte la marina de guerra*. https://www.infobae.com/peru/2023/05/27/oleaje-anomalo-llegara-a-su-punto-pico-este-fin-de-semana/

Mann, H. B., & Whitney, D. R. (1947). On a test of whether one of two random variables is stochastically larger than the other. *The Annals of Mathematical Statistics*, *18*(1), 50–60. https://doi.org/10.1214/aoms/1177730491

Müller, G. V., & Ambrizzi, T. (2007). Teleconnection patterns and rossby wave propagation associated to generalized frosts over southern south america. *Climate Dynamics*, *29*, 633–645. https://doi.org/10.1007/s00382-007-0253-x

Otiniano, J. R. (2006). Oleajes anómalos y su impacto en zonas costeras [Bitácora Hidrográfica (N.º 2, pp. 11–13). Dirección de Hidrografía y Navegación de la Marina de Guerra del Perú]. https://www.dhn.mil.pe/Archivos/bitacora/edc_02.pdf

Smirnov, N. V. (1948). Table for estimating the goodness of fit of empirical distributions. *The Annals of Mathematical Statistics*, *19*(2), 279–281. https://doi.org/10.1214/aoms/1177730256

Stewart, R. H. (2008). Introduction to physical oceanography (capítulo 16: Ocean waves). https://ocean.tamu.edu/Faculty/Stewart/intro_oc.html

Tamayo Infantes, M. (2007). Oleaje anómalo de fuerte intensidad en la bahía de miraflores [Bitácora Hidrográfica, (03), 13–16. Dirección de Hidrografía y Navegación de la Marina de Guerra del Perú]. https://www.dhn.mil.pe/Archivos/bitacora/edc_03.pdf

Virtanen, P., Gommers, R., Oliphant, T. E., Haberland, M., Reddy, T., Cournapeau, D., ..., & Contributors, S. 1. (2020). Scipy 1.0: Fundamental algorithms for scientific computing in python. *Nature Methods*, *17*(3), 261–272. https://doi.org/10.1038/s41592-019-0686-2

Appendix A: Sequences of Wind Fields at 250 hPa, Geopotential Height at 500 hPa, Surface Pressure, and Surface Wind

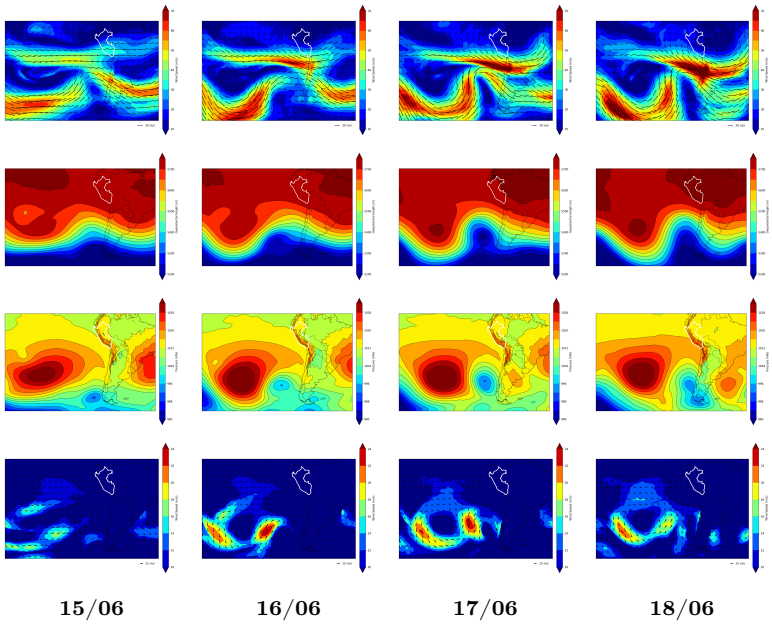

Figure A1: *Sequences of wind fields at 250 hPa (first row), geopotential height at 500 hPa (second row), surface pressure (third row), and surface wind (fourth row) for the days preceding the onset of event E1 (19/06/2011), obtained from ERA5 reanalysis data.*

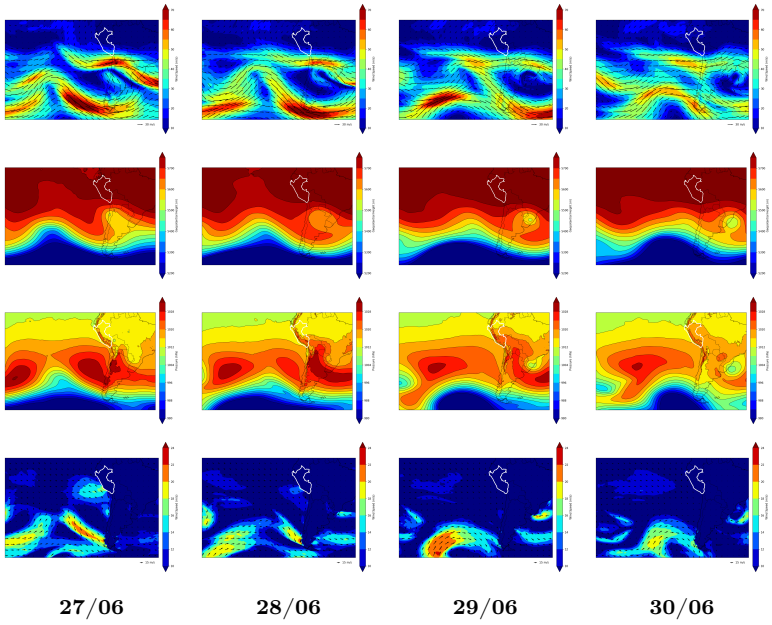

Figure A2: *Sequences of wind fields at 250 hPa (first row), geopotential height at 500 hPa (second row), surface pressure (third row), and surface wind (fourth row) for the days preceding the onset of event E2 (01/07/2014), obtained from ERA5 reanalysis data.*

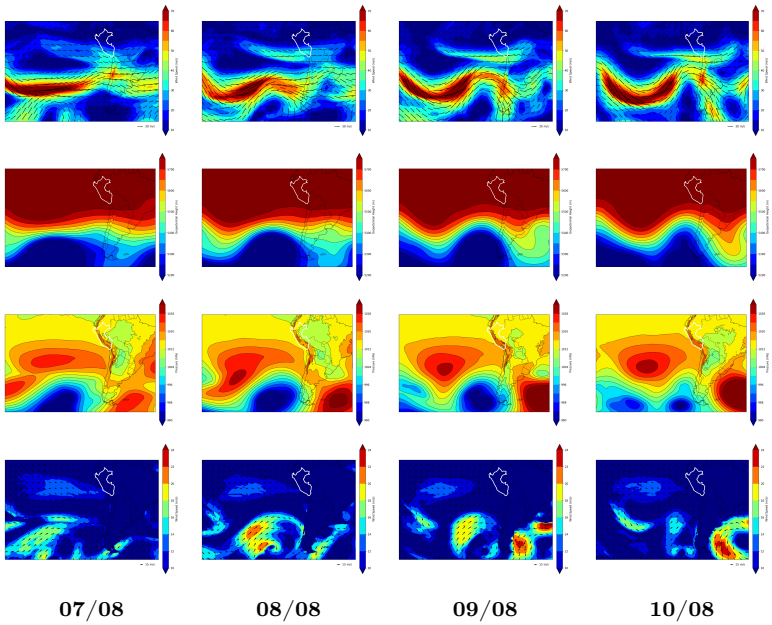

Figure A3: *Sequences of wind fields at 250 hPa (first row), geopotential height at 500 hPa (second row), surface pressure (third row), and surface wind (fourth row) for the days preceding the onset of event E3 (11/08/2017), obtained from ERA5 reanalysis data.*

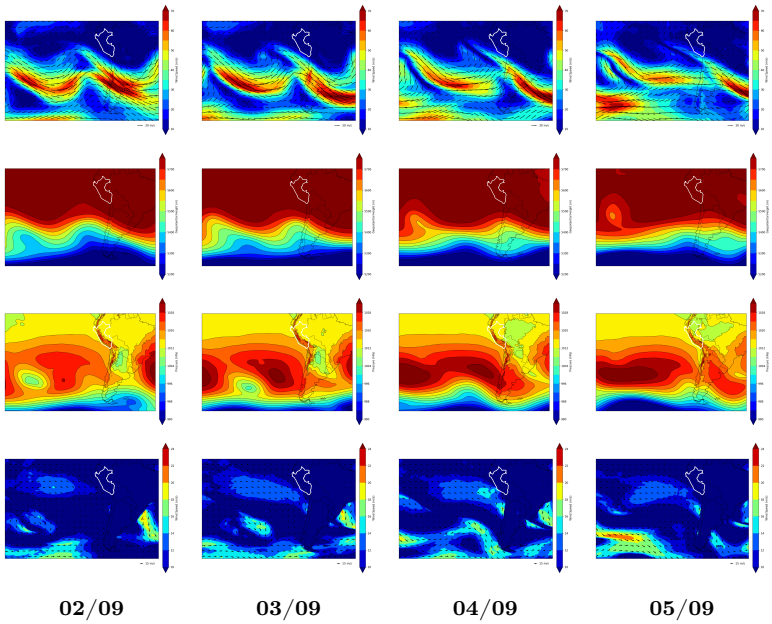

Figure A4: *Sequences of wind fields at 250 hPa (first row), geopotential height at 500 hPa (second row), surface pressure (third row), and surface wind (fourth row) for the days preceding the onset of event E4 (07/09/2017), obtained from ERA5 reanalysis data.*

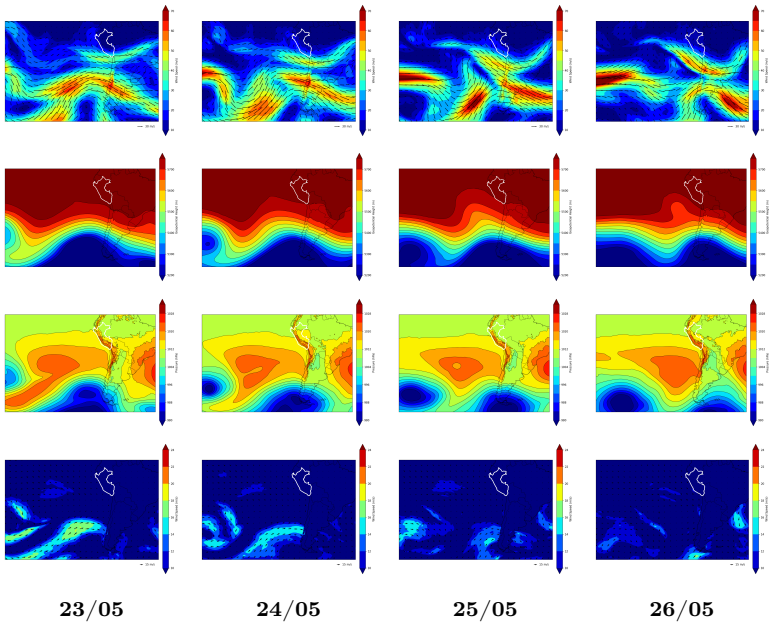

Figure A5: *Sequences of wind fields at 250 hPa (first row), geopotential height at 500 hPa (second row), surface pressure (third row), and surface wind (fourth row) for the days preceding the onset of event E5 (27/05/2023), obtained from ERA5 reanalysis data.*

Event	Fetch central coordinates	Coordinates of the average point
E1	40ºS – 93ºW	**44ºS, 101.6ºW**
E2	55ºS – 115ºW	
E3	40ºS – 105ºW	
E4	45ºS – 100ºW	
E5	40ºS – 95ºW	

Table A1: *Geographic coordinates of the central points within the region where the most intense "fetch" occurred for each "very strong" swell event. To the right, the coordinates of the average point, obtained by calculating the arithmetic mean of the individual fetch centers, are shown. This average point was used to estimate a reference distance for the calculation of wave train arrival time.*

Appendix B: Time Series of Principal Components from Surface Pressure, 500 hPa Geopotential, and 250 hPa Geopotential Fields

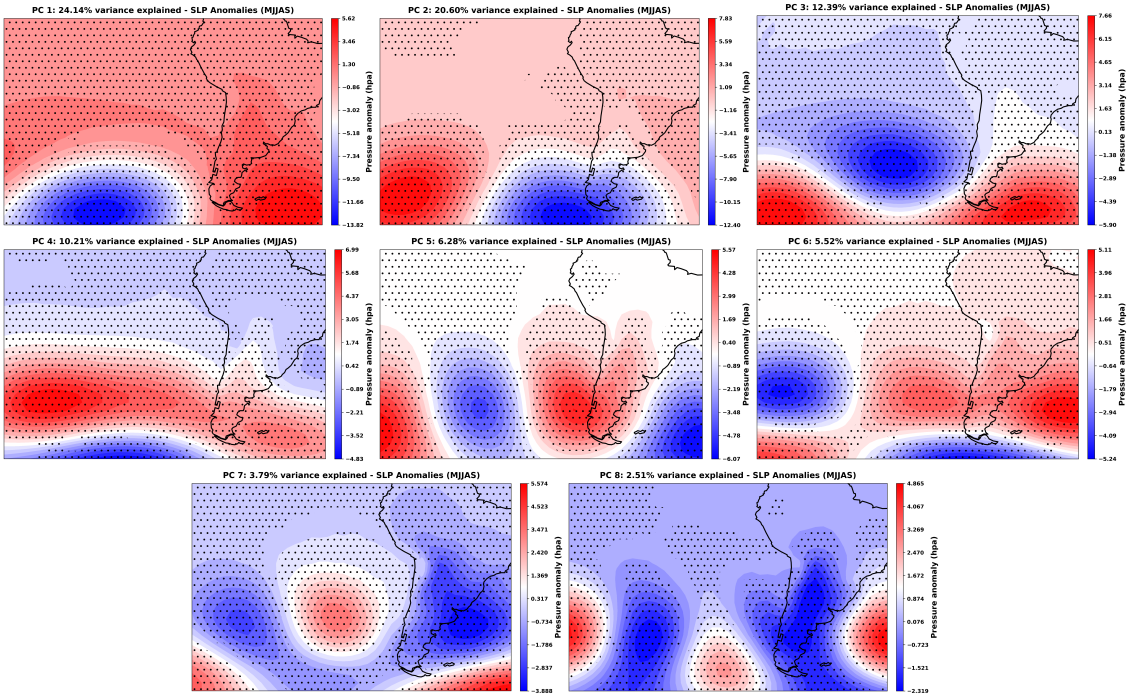

Figure B1: *Regression maps corresponding to the first eight Principal Components (PC1 to PC8) of the daily sea level pressure (SLP) anomaly field, calculated for the months of May through September (MJJS) from 1991 to 2023. Stippled areas indicate statistical significance ($p < 0.05$) based on the Mann–Whitney U test.*

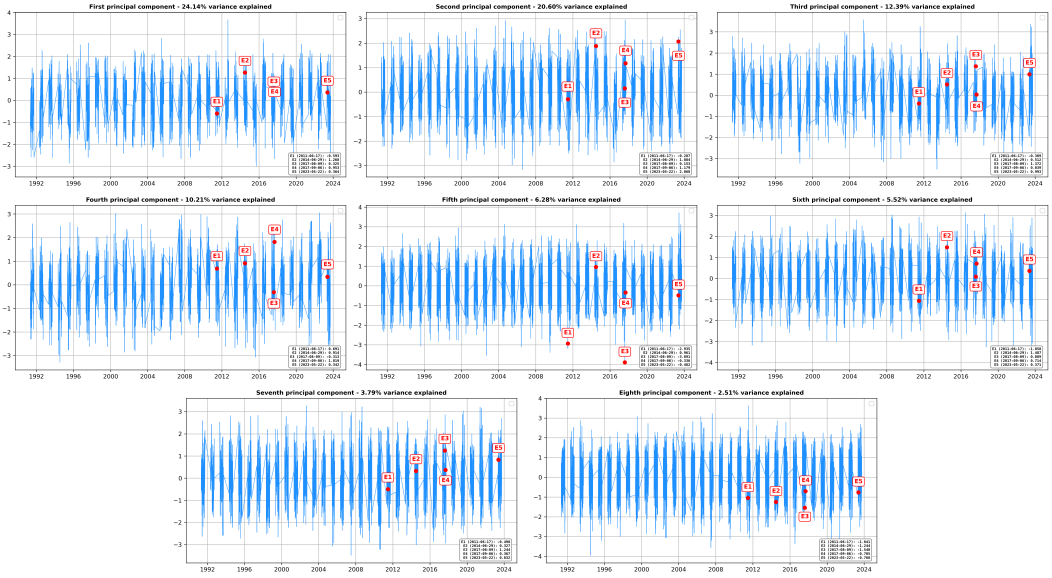

Figure B2: *Time series of the first eight principal components (PC1–PC8) of the daily sea level pressure (SLP) anomaly field, calculated for the months of May to September (MJJS) between 1991 and 2023. Red values correspond to the five extreme events (E1–E5) for each time series, as detailed in the bottom-right panel.*

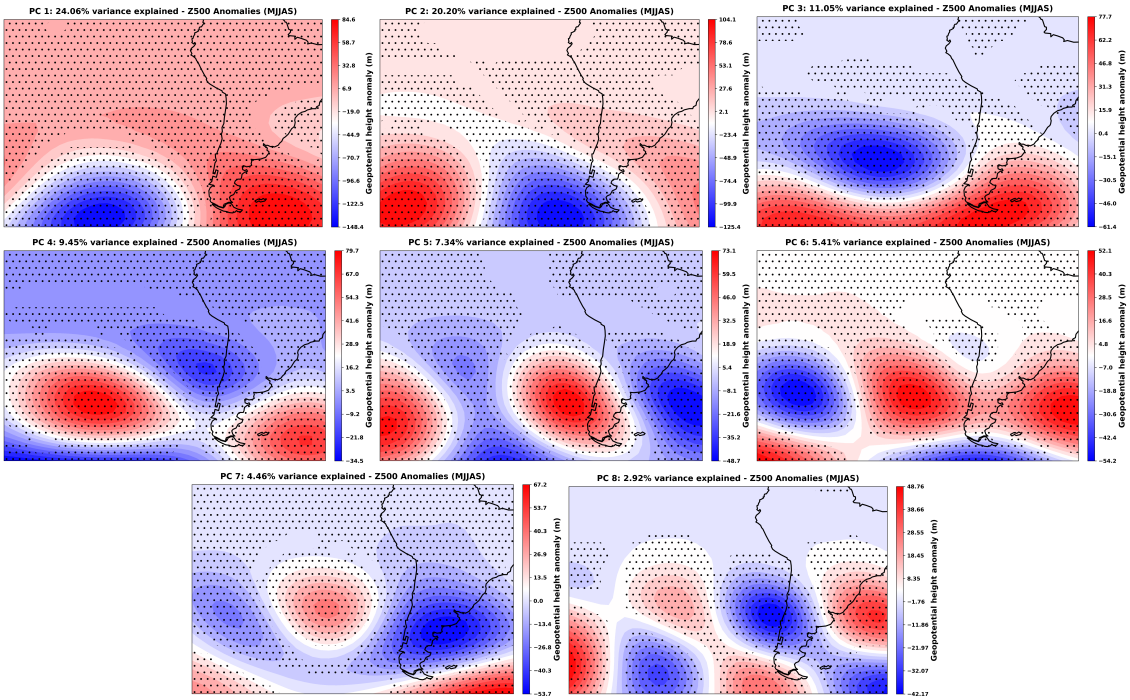

Figure B3: *Regression maps corresponding to the first eight principal components (PC1–PC8) of the daily 500 hPa geopotential height anomaly field, calculated for the months of May to September (MJJS) between 1991 and 2023. Stippled areas indicate statistical significance ($p < 0.05$) based on the Mann–Whitney U test.*

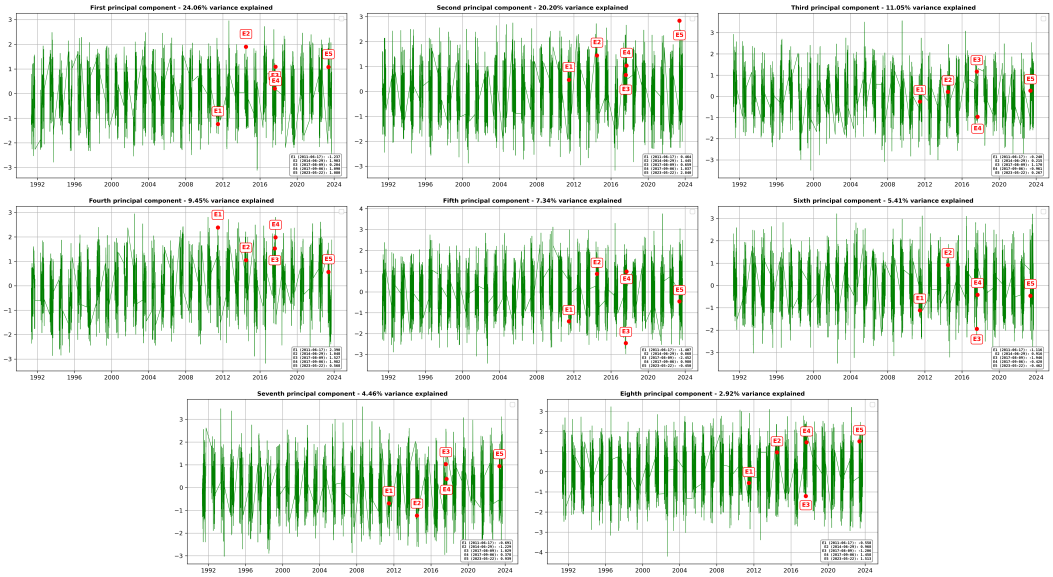

Figure B4: *Time series of the first eight principal components (PC1–PC8) of the daily 500 hPa geopotential height anomaly field, calculated for the months of May to September (MJJS) between 1991 and 2023. Red values correspond to the five extreme events (E1–E5) for each time series, as detailed in the bottom-right panel.*

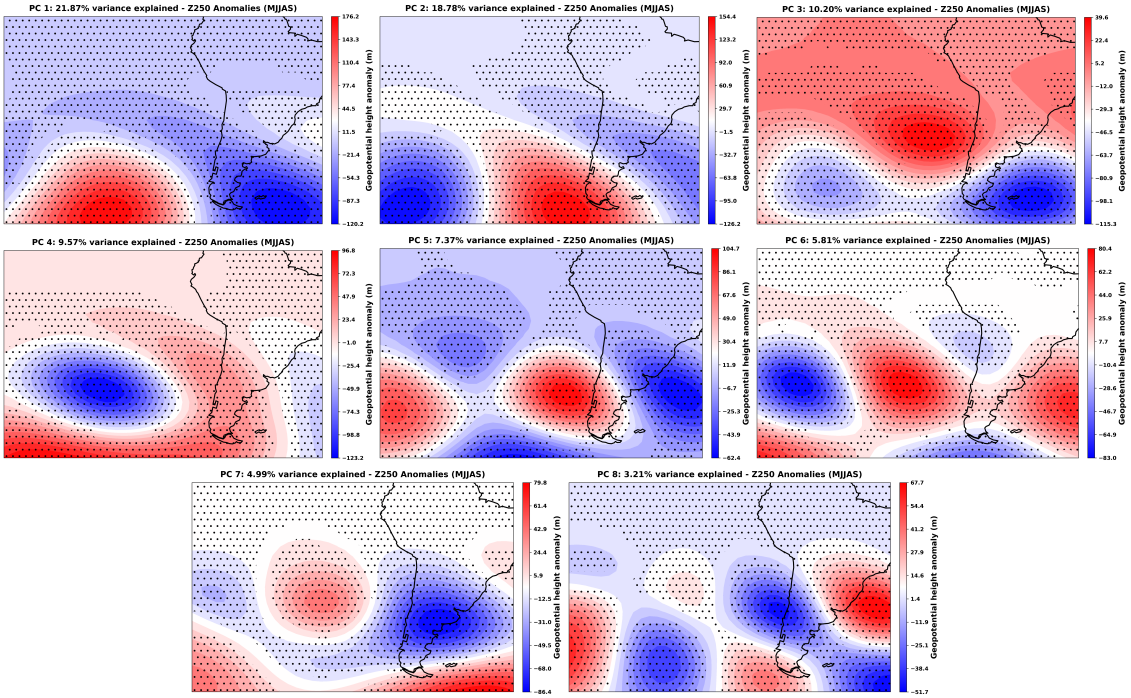

Figure B5: *Regression maps corresponding to the first eight principal components (PC1–PC8) of the daily 250 hPa geopotential height anomaly field, calculated for the months of May to September (MJJS) between 1991 and 2023. Stippled areas indicate statistical significance ($p < 0.05$) based on the Mann–Whitney U test.*

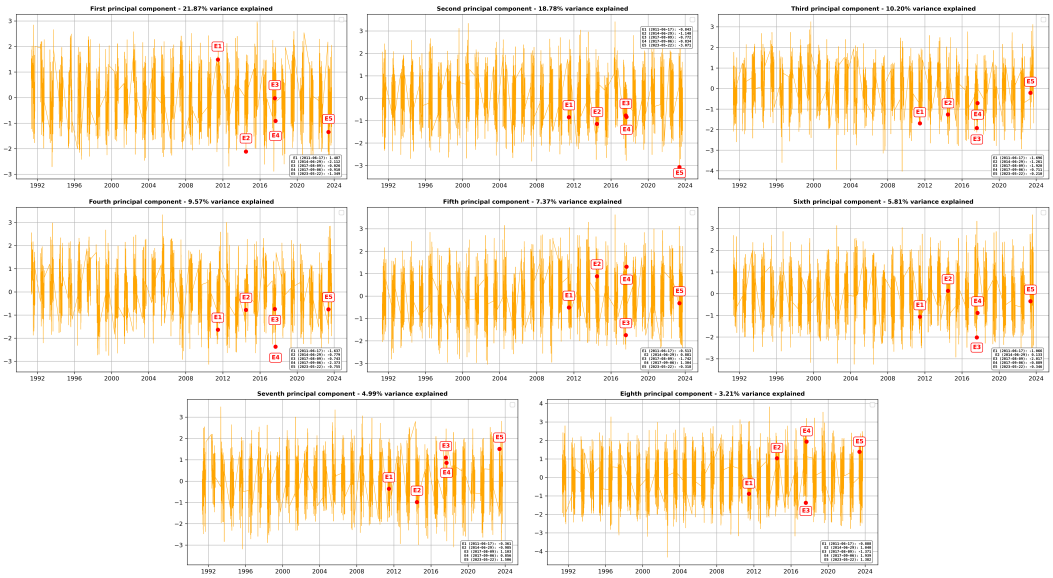

Figure B6: *Time series of the first eight principal components (PC1–PC8) of the daily 250 hPa geopotential height anomaly field, calculated for the months of May to September (MJJS) between 1991 and 2023. Red values correspond to the five extreme events (E1–E5) for each time series, as detailed in the bottom-right panel.*